Chemical Engineering Journal 518 (2025) 164494

Contents lists available at ScienceDirect

Chemical Engineering Journal

journal homepage: www.elsevier.com/locate/cej

Advanced NiMoC electrocatalysts precision synthesised at room temperature for efficient hydrogen evolution across pH ranges

Farid Attar [a], Asim Riaz [a,*], Doudou Zhang [b,*], Haijiao Lu [c], Lars Thomsen [d], Siva Karuturi [a,*]

[a] School of Engineering, The Australian National University, Canberra, Australian Capital Territory, 2601, Australia
[b] School of Engineering, Macquarie University, Sydney, New South Wales 2109, Australia
[c] Nanomaterials Centre, School of Chemical Engineering, and Australian Institute for Bioengineering and Nanotechnology, The University of Queensland, St Lucia, QLD 4072, Australia
[d] Australian Synchrotron, ANSTO, 800 Blackburn Road, Clayton, VIC 3168, Australia

ARTICLE INFO

Keywords:
Magnetron sputtering
Room temperature synthesis
Hydrogen evolution reaction
Multi-metallic carbide
pH-universal

ABSTRACT

Transition metal-based multi-metallic carbides are promising electrocatalysts for hydrogen evolution due to their catalytic properties. Synthesis is challenging due to agglomeration, scalability limits at high temperatures, and impurities. This study introduces a room-temperature, one-step magnetron co-sputtering technique to fabricate NiMoC electrocatalysts, achieving uniform carbon deposition with Ni and Mo. Integrating a carbon magnetron source with transition metals forms unique bonds, with controlled composition and thickness, enhancing catalytic performance. NiMoC demonstrates outstanding performance in alkaline conditions, with overpotentials of 26 mV at 10 mA cm^{-2} and stability over 10 days. This represents that introducing a separate carbon source during magnetron co-sputtering improves NiMoC overpotential by 62.8 % at 10 mA cm^{-2} compared to NiMo. These enhancements stem from Mo_2C and NiMo active sites, and improved conductivity and stability from disordered and graphite-like carbon. Sputtered NiMoC exhibits remarkable performance across pH levels, with 42 mV overpotential at 10 mA cm^{-2} and stability over 70 h in acidic conditions. When integrated into a zero-gap electrolyser, NiMoC achieves excellent cell voltages of 1.78 V at 0.5 A cm^{-2} and 1.87 V at 1 A cm^{-2}, maintaining stability for 68 h. These findings highlight magnetron co-sputtering's potential for room-temperature synthesis of multi-metallic carbides, advancing energy conversion.

1. Introduction

The rising global energy crisis and environmental pollution, caused by fossil fuel overuse, have created a significant demand for renewable and clean energy alternatives. [1] Among these, green hydrogen energy stands out for its remarkable energy density and versatile applications. [2,3] A sustainable method to produce green hydrogen is electrochemical water splitting, potentially utilising carbon-free energy sources [4]. Efforts are focused on developing earth-abundant catalysts for hydrogen evolution reactions (HER) and oxygen evolution reactions (OER) to decrease dependence on precious metals, making electrochemical water splitting feasible on an industrial scale. [5,6]

Significant attention has been dedicated to advancing multi-metallic catalysts owing to their tunable electronic structures, which offer the potential for enhanced catalytic performance. Among these, NiMo alloys have shown particular promise as catalysts for HER due to their strong water adsorption and efficient hydrogen desorption capabilities. [7,8] To further enhance the performance of NiMo-based catalysts, the incorporation of carbides offers a potential pathway for improvement, leading to the formation of transition metal-based multi-metallic carbides (TMMCs). [9] These TMMCs showcase compelling qualities for HER reactions, demonstrating exceptional performance and stability, often in diverse pH conditions. [10] Additionally, they possess high ionic and metallic conductivity, along with notable melting points and corrosion resistance. [11] Yu et al. [12] synthesised various TMMCs by introducing different transition metals into molybdenum carbides and assessed their HER performance. Their findings revealed that Ni-Mo_2C emerged as the most effective catalyst among Co-Mo_2C, Fe-Mo_2C, and Cr-Mo_2C, primarily due to its superior hydrogen desorption capability. The development of TMMCs presents significant challenges, due to the high synthesis temperatures needed to overcome thermodynamic and kinetic barriers. [13] At elevated temperatures, particle agglomeration

---

[*] Corresponding authors.
E-mail addresses: Asimriaz.anu@gmail.com (A. Riaz), doudou.zhang@mq.edu.au (D. Zhang), siva.karuturi@anu.edu.au (S. Karuturi).

https://doi.org/10.1016/j.cej.2025.164494
Received 11 March 2025; Received in revised form 22 May 2025; Accepted 3 June 2025

can become a concern, reducing the catalytic surface area. Also, fabricating effective TMMC electrodes typically involves multiple synthesis steps, especially in solution-based methods, which can introduce impurities and generate various by-products. [10] Therefore, introducing a one-step deposition method capable of synthesising controlled TMMCs at room temperature is crucial for practical applications in water splitting.

Magnetron sputtering, a solution-free and physical vapour deposition method, presents the ability to fabricate TMMCs catalysts at room temperature. [14] Recently, our team demonstrated the potential of magnetron sputtering to develop efficient HER and OER catalysts, such as Ni_3N and NiFeMoN. [15,16] This technique is cost-effective and repeatable, making it ideal for water electrolysis applications. [17] Co-sputtering enables the simultaneous deposition of multiple components, ensuring uniform composition and precise control across substrates, even with triple targets. This technique enhances material properties and overall performance. [15,18] To date, only one study has explored the use of sputtered Ni-doped Mo_2C for HER water splitting. [19] In that work, Ni and Mo_2C were employed as targets, limiting the catalyst's optimisation, particularly in terms of carbon's role in the catalytic process. [20] Additionally, the absence of distinct Mo and graphite targets limited the formation of the NiMo alloy, graphite, and disordered carbon. These limitations reduced the catalytic effectiveness of this catalyst compared to other superior ones, especially at high current densities. It is noteworthy that, to date, no successful attempts have been made to fabricate TMMCs as catalysts using triple-target magnetron co-sputtering for water electrolysers.

In this study, we developed a novel NiMoC catalyst using triple-target magnetron co-sputtering for HER in water splitting at room temperature. The optimised NiMoC exhibits outstanding performance across a wide pH range, achieving ultralow overpotentials of 26 mV and 42 mV at 10 mA cm^{-2} in alkaline and acidic conditions, respectively. Moreover, it demonstrates remarkable stability, maintaining its efficiency for 10 days in alkaline media and 70 h in acidic environments. Material characterisations reveal the generation of Mo_2C, NiMo, disordered carbon, and graphite-like carbon, which contribute to increased active sites and improved electrical conductivity. Additionally, high current density tests in a zero-gap electrolyser revealed the low cell voltage of 1.78 V and 1.87 V at high current density of 0.5 A cm^{-2} and 1 A cm^{-2} indicating suitability for practical applications. This study provides a promising pathway for the precise fabrication of high-performance TMMC catalysts at room temperature using a facile and scalable synthesis method.

2. Materials and methods

2.1. Catalyst fabrication

Two 3 mm-thick layers of Ni foam were uniformly compressed to form a 0.5 mm-thick pressed Ni foam (PNF). This PNF was subjected to a thorough cleaning process involving sequential ultrasonication in ethanol, acetone, 3.0 M diluted HCl, and deionised water, each step lasting for 10 min. NiMoC was deposited onto the PNF using direct current mode of triple-targets magnetron co-sputtering (ATC 2400, AJA International Inc.). The process was carried out at room temperature and a constant chamber pressure of 4 mTorr, with a continuous substrate rotation and a steady argon flow of 20 sccm to ensure uniform deposition. Mo (99.99 %), Ni (99.99 %), and graphite (99.99 %) targets were utilised, with a steady flow of 20 sccm of argon gas maintained in the chamber during deposition.

The power settings for the Mo, Ni, and graphite targets were individually adjusted to a maximum of 150 W to optimise the catalytic composition, while the sputtering deposition time was precisely controlled to achieve the desired catalyst thickness. It is important to note that when developing NiMo, NiC, and MoC catalysts, the graphite, Mo, and Ni targets, respectively, remain unignited, while the remaining targets operate at the optimal power level required for NiMoC.

To ensure consistent film adhesion across all samples, the sputtering conditions—including pressure, gas flow, substrate rotation, and deposition temperature—were kept identical. Magnetron sputtering inherently promotes strong adhesion through energetic ion bombardment, enabling the formation of dense and adherent catalyst films. Additionally, all samples were deposited on the same PNF substrate, and deposition time and target powers were carefully controlled to maintain comparable film thicknesses.

In order to compare the Pt catalyst with NiMoC, the magnetron sputtering process was conducted at 150 W with 100 % Ar flow, utilising a Pt sputtering target. The pressure was maintained at a constant 4 mTorr, and the deposition was carried out at room temperature. The total deposition time was fixed to achieve a Pt film thickness of 700 nm.

2.2. Material characterisation

Different material characterisation was conducted, encompassing X-ray diffraction (XRD), energy-dispersive spectroscopy (EDS), scanning tunneling electron microscopy (STEM), and scanning electron microscopy (SEM), all using Si/SiOx and PNF substrates. The crystallinity of catalysts was determined by XRD (PANalytical X'Pert PRO MRD), utilising Cu Kα radiation ($\lambda = 1.540598$) and a scan range of 10–80°. Grazing incidence XRD was conducted at an incident angle of 2°. The morphology of NiMo and NiMoC was examined by STEM (JEOL JEM-ARM200F) and surface and cross-sectional scanning electron microscopy (SEM, FEI Helios 600 NanoLab, accelerating voltage of 200 V–30 kV). Using inductively coupled plasma mass spectrometry (ICP-MS, Agilent Technologies 7700), the weight percentages of Ni and Mo were determined.

Surface chemical properties of catalysts were explored through X-ray photoelectron spectroscopy (XPS) using a Thermo ESCALAB250Xi, calibrated to a C1s reference peak. Raman spectra were obtained with a Renishaw Raman microscope using a 532 nm laser, operating at 5 mW power, and utilising a 50× lens. C K-edge X-ray absorption near edge structure (XANES) measurements are performed at the Soft X-ray beamline located in Australian Synchrotron in Melbourne, Australia. The photon range of the beamline encompasses the XANES C K-edge at high resolution >10,000. The absorption spectra of the samples were obtained through the Total Electron Yield (TEY) signal, measured as the drain current. To assess wettability, we employed an automated water dropper and goniometer to measure the water contact angle. A small droplet was carefully dispensed onto surfaces coated with NiMo and NiMoC, both deposited onto Ni-coated silicon.

2.3. Electrochemical measurement in acidic and alkaline condition

Using a potentiostat (Autolab PGSTAT302N), electrochemical measurements in acidic, neutral and basic conditions were systematically performed within a three-electrode setup, where the sputtered catalysts electrode, Pt and the saturated calomel electrode (SCE) were employed as working, counter and reference electrodes. For all electrochemical tests, the distance between the three electrodes was kept constant. Eq. 1 as shown below was employed to convert the recorded potentials to the reversible hydrogen electrode (RHE) scale:

$$V_{RHE} = V_{SCE} + 0.241\ V + 0.059 \times pH_{electrolyte} \tag{1}$$

where pH values are 13.5, 7.4 and 0 in alkaline and acidic environments, respectively. Linear sweep voltammetry (LSV) measurements were carried out in 0.5 M H_2SO_4 1 M (Phosphate buffered saline) PBS and 1 M KOH with a sweep rate is 5 mV s^{-1}. Electrochemical Impedance Spectroscopy (EIS) measurements were performed within a frequency range from 0.1 to 100 kHz. These measurements were conducted at an overpotential of 10 mA cm^{-2} in both acidic and basic conditions. To compare the double-layer capacitance (C_{dl}) of NiMo and NiMoC, the non-faradaic region between 0.1 and 0.3 V (RHE) was selected. [21] The scan rate was incrementally increased from 5 to 200 mV s^{-1} for this purpose. To investigate charge transfer and side reactions, we employed multi-current chronopotentiometry. The procedure was commenced at 50 mA cm^{-2}, increasing by 50 mA cm^{-2} every 5 min until reaching 300 mA cm^{-2}. Then, we reversed the process to return to 50 mA cm^{-2}.

2.4. Zero-gap electrolyser measurements

We employed NiFeCo, previously developed by our group, [22] and Fumapem FA-3-50 as an anionic membrane as the anode and membrane, respectively, in the zero-gap electrolyser setup. The cathode consisted of our as-developed NiMoC synthesised via magnetron sputtering and deposited on PNF. Serpentine flow field Ni electrode plates, sized at 5 cm^2, were sourced from Dioxide Materials™ and utilised in the zero-gap electrolyser. The Teflon gaskets used to sandwich the electrodes have a 1 cm^2 opening flow window, which limits the active area for electrolysis to 1 cm^2. This design ensures that the electrolysis reaction occurs within the specified active region, while the larger electrode plates (5 cm^2) provide structural support and better electrolyte and current distribution. Before being sandwiched between the OER and HER electrodes with the Teflon gaskets, the membrane was activated by immersing it in a 1 M KOH solution for 24 h. The electrolyte, with a 1 M KOH concentration at varying temperatures, was introduced into the anode and cathode plates at a controlled flow rate of 3 ml min^{-1}, via a BT600LC pump. These plates were then linked to the working and counter electrode terminals for electrochemical assessment conducted using a potentiostat (Autolab PGSTAT302N).

3. Result and discussion

3.1. NiMoC synthesis by triple targets magnetron co-sputtering

To synthesise NiMoC on PNF, we used room-temperature triple-target magnetron co-sputtering where graphite, Ni and Mo targets are in a confocal configuration toward the substrates (Fig. 1). In this method, Ni, Mo and C particles are ejected from targets and travel toward the PNF. During the process, some of the sputtered Mo atoms react with carbon to form MoC, a stable phase due to its relatively large negative standard enthalpy of formation ($\Delta H^0 \approx -27$ kJ/mol). In contrast, the formation of nickel carbide is thermodynamically less favorable, as indicated by its small positive enthalpy of formation ($\Delta H^0 \approx +1.2$ kJ/mol) under standard conditions. [23] However, metastable NiC can still form temporarily under non-equilibrium deposition conditions. As reported by Suzko et al. [24], such metastable phases may form during sputtering and can later decompose at or near the substrate surface. On the other hand, sputtered Ni atoms react with MoC particles, leading to the formation of NiMoC. According to the growth mechanism proposed by Jansson and Lewin for bimetallic carbide systems containing one strong carbide former (e.g., Mo) and one weak carbide former (e.g., Ni), an initial NiMoC ternary phase may form, which could subsequently decompose into NiMo-MoC. [25] In addition, the process also produces disordered carbon and a graphitic structure, as observed in recent sputtered depositions. [26–28]

The flexibility of magnetron sputtering, especially with a separate carbon source, allows us to finely tune both the targets' power and deposition time, providing more control over the catalyst's composition, elemental ratios, and the thickness of the catalyst layer. This level of control is essential for optimising NiMoC and introducing the role of carbon in HER reaction. The following sections will delve into the analysis of NiMo, Mo_2C, disordered carbon and graphitic structures using various characterisation tests. A more detailed description of the magnetron sputtering deposition process can be found in the Materials and Methods section.

3.2. Characterisation of NiMoC electrocatalyst

We deposited an earth-abundant NiMoC on PNF and SiO_x/Si using triple-target magnetron co-sputtering to examine its morphology and material characteristics. The cross-section SEM image of NiMoC deposited on SiO_x/Si reveals a nanorod-shaped structure with a thickness of 700 nm (Fig. 2a). This morphology shows promise for enhancing catalytic surface area and adsorption of reactants, potentially improving overall performance. [15,16] SEM images of NiMo and NiMoC on PNF reveal a uniform and densely packed layer of catalysts, with no observable alteration in morphology after the addition of the carbon target (Figs. S1a and S1b) in the magnetron process. Furthermore, the top-view SEM images (Figs. S1b inset and S1c) of NiMoC deposited on both PNF and SiO_x/Si reveal a granular structure with an average size of 10 nm. These nanogranular morphologies have the potential to boost reactivity for the HER, facilitate mass transport, and improve catalyst stability. [10,29]

No extra peaks are observed when comparing the XRD patterns of NiMoC and NiMo with PNF, which shows a polycrystalline face-centred-

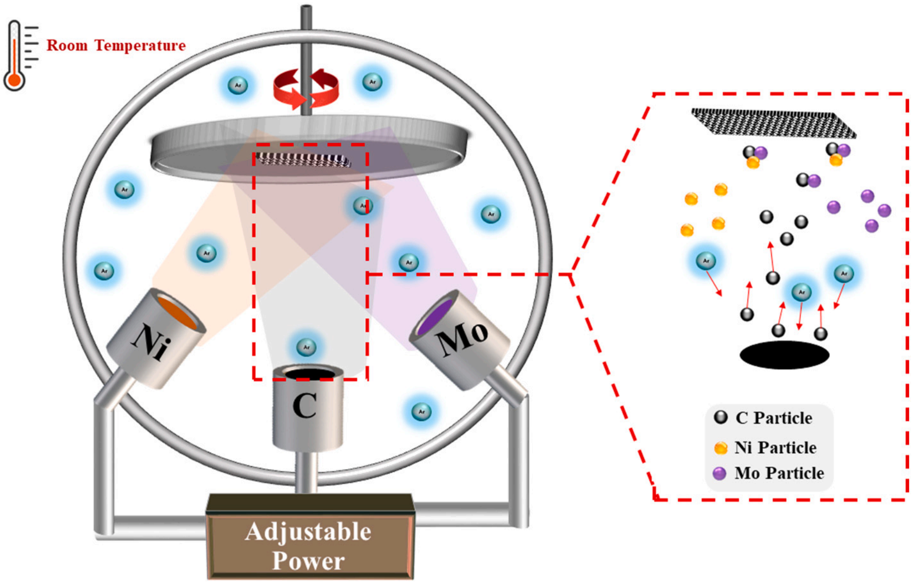

Fig. 1. Schematic of NiMoC deposition by room temperature triple-targets magnetron co-sputtering.

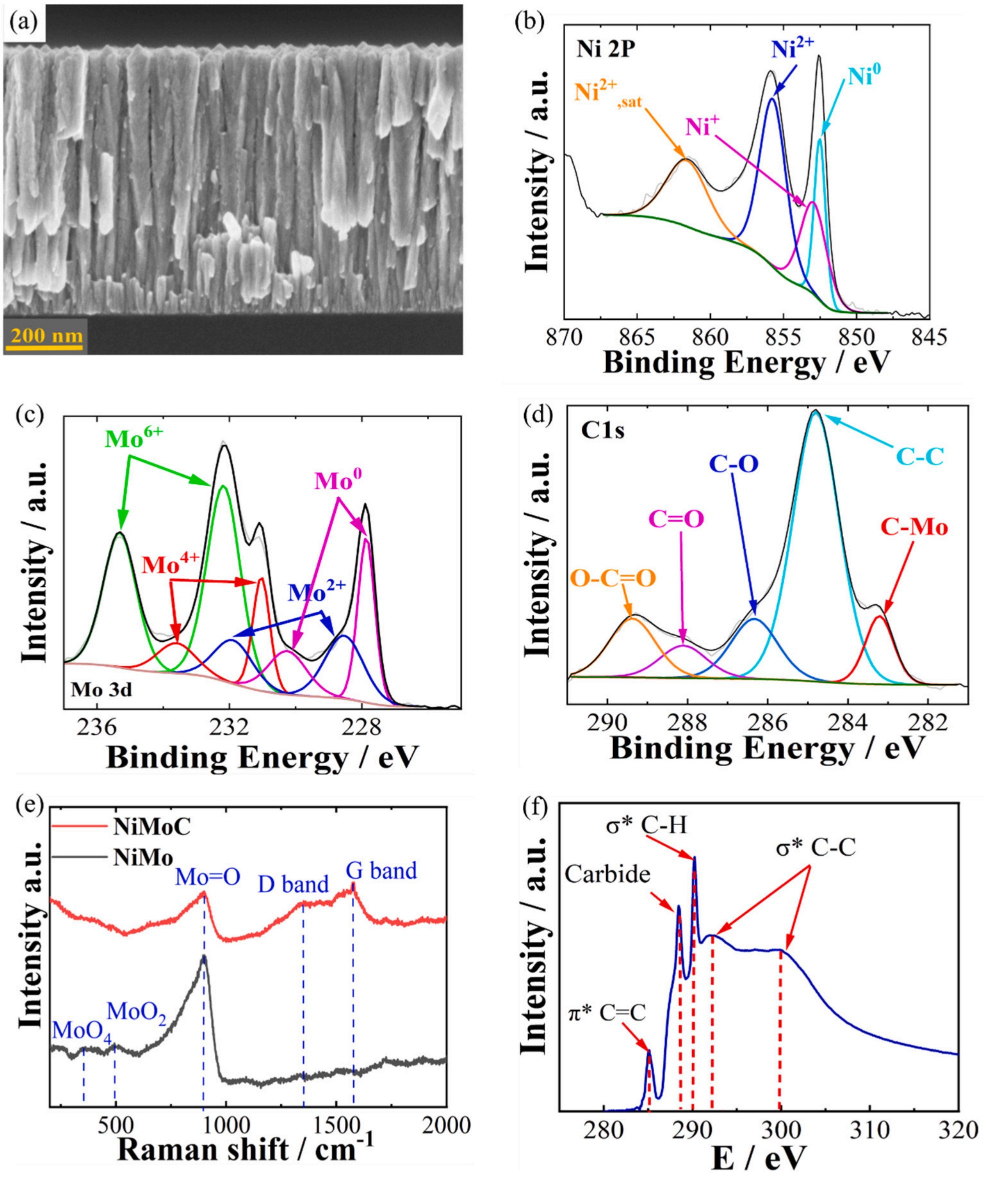

Fig. 2. (a) Cross-section SEM images of NiMoC. XPS spectra (b) Ni 2p, (c) Mo 3d, (d) C 1 s in NiMoC. (a) Raman spectrum of NiMo and NiMoC. (f) C K-edge XANES spectra of NiMoC.

cubic (fcc) Ni structure (Fig. S2, JCPDS # 04–0850). Grazing Incidence XRD (GIXRD) was applied to analyse the sputtered film's crystallinity while minimising the substrate's influence (SiO_x). The results show a polycrystalline face-cantered-cubic (fcc) Ni structure with no detectable peaks of Mo_2C (Fig. S3). STEM and SAED analysis reveal the amorphous structure of NiMoC, consistent with findings from previous magnetron-sputtered catalysts (Fig. S4). [14,15] Moreover, STEM analysis indicates a dispersed graphitic structure, suggesting that magnetron sputtering may produce graphite, which could significantly enhance HER performance by improving conductivity. [30–32] Elemental mapping of NiMoC in both cross-section and top view (Fig. S5) illustrates the uniform distribution of Ni, Mo, and C on the substrates, with Ni being predominant. This confirms that triple-target magnetron co-sputtering can uniformly deposit multi-component materials onto various substrates.

To evaluate the surface properties and chemical valence states, X-ray photoelectron spectroscopy (XPS) is conducted on NiMoC, revealing the coexistence of Ni, Mo, and C in the catalysts. The Ni 2p spectrum in Fig. 2b corresponds to Ni^0 (852.4 eV), Ni^+ (853 eV and), Ni^{2+} (855.8 eV) and a satellite peak named “sat.” ($Ni^{2+}_{,}$ sat at 861.6). [12,33,34] Comparing Ni 2p spectra of NiMoC and NiMo (Fig. S6a) reveals increased intensity of the metallic Ni peak upon the addition of carbon, which can improve the HER performance. [35] The Mo 3d spectrum deconvolves into Mo^0 (227.8 eV and 230.3 eV), Mo^{2+} (228.6 eV and 232.0 eV), Mo^{4+} (231.0 eV and 233.6 V) and Mo^{6+} (232.2 eV and 235.3 eV). [12,34,36] The presence of Mo^{4+} and Mo^{6+} may be attributed to surface Mo oxidation. However, these oxidised Mo atoms tend to thermodynamically undergo electro-reduction during water splitting, which can then serve as active sites. [37,38] Comparing the Mo 3d spectra of NiMo and NiMoC in Fig. S6b reveals an increase intensity of Mo^0 upon the incorporation of carbon. The high intensity of metallic Mo can further modify the electronic structure and surface properties of the catalyst, ultimately reducing the energy barrier for the HER reaction. [39] Additionally, the Mo^{2+} peaks exhibit a low binding energy shift with the addition of carbon, indicating charge transfer from carbon to molybdenum. This charge donation enhances the electron density surrounding the Mo atoms and implies the possible formation of Mo—C bonds. [10] In contrast, the Ni 2p peaks exhibit no sensible shifts, indicating a less significant interaction between nickel and carbon. This disparity suggests that the charge transfer predominantly occurs between Mo and C, favouring the formation of Mo—C over Ni—C bonds—a trend that aligns with previous reports. [24] This preference can be attributed to the thermodynamic stability of Mo—C, which has a relatively large negative standard enthalpy of formation ($\Delta H^0 \approx -27$ kJ/mol), compared to the slightly positive value for Ni—C ($\Delta H^0 \approx +1.2$ kJ/mol). Furthermore, according to Jansson and Lewin, metastable Ni—C bonds may eventually decompose near the substrate surface in the presence of a strong carbide former such as Mo. [25] This charge transfer can weaken the strong Mo—H bonds, facilitating the desorption of H_2 and resulting in improved HER performance. [40]

Fig. 2d and S4c display the XPS spectrum of C1s, with the peak at 284.8 eV serving as a calibration reference throughout the experiment for all XPS spectra. The presence of oxygen-containing hydrocarbons, such as O-C=O, C=O, and C—O detected at 289.4 eV, 288.1 eV, and 286.3 eV respectively, indicates surface contamination by airborne carbon on the sample. [36,41] The peak at 283.4 corresponds to a carbide bond. Given the negative shift of Mo^{2+} (Fig. S6b) and less favorable formation of Ni—C, this peak suggests the presence of Mo—C in the NiMoC catalyst (Fig. S6c). [33,36] Moreover, while the peak at 284.8 is commonly used as a reference peak, the increased peak intensity in NiMoC compared with NiMo indicates graphite and disordered carbon generation in the NiMoC catalyst. [42,43] The O 1 s spectra of NiMo and NiMoC are deconvoluted into three subpeaks, including adsorbed H_2O (H_2O_{ads}, 533 eV), metal hydroxide (M-OH, 531.3 eV) and adsorbed oxygen (M-O, 530 eV), as shown in Fig. S6d. [44] The relative intensities of the subpeaks indicate that the addition of carbon enhances the content of metal hydroxide (M-OH), thereby improving wettability. [36] We further measure the water contact angles to assess the wettability of both NiMoC and NiMo. Enhanced wettability indicates superior adsorption of water molecules on catalysts, a crucial step in the water-splitting reaction. [16] Fig. S7 illustrates a lower contact angle for NiMoC (47.9°) compared to NiMo (64.8°), indicating improved wettability after co-sputtering with carbon. Further, we determined the atomic ratio of Ni:Mo:C in NiMoC based on the XPS peaks of Ni 2p, Mo 3d, and the C 1 s (peak at 283.4), which resulted in a ratio of 11.1:2.2:1.

Fig. 2e shows the Raman spectra of NiMo and NiMoC. The peaks at 378 cm^{-1}, 492 cm^{-1}, and 898 cm^{-1} are attributed to MoO_4, MoO_2, and M = O, respectively, resulting from the surface oxidation of Mo. [45–48] Comparing NiMoC with NiMo, we observe a reduction in these peaks due to carbon addition, indicating enhanced resistance to oxidation. In addition, the D band (1580 cm^{-1}) and G band (1350 cm^{-1}) are visible in the Raman spectra of NiMoC. The D band signifies the presence of structural imperfections and disorder, while the G band originates from the stretching of the C—C bond in graphitic material. [12] The ratio of their intensity (I_G/I_D) is 1.25 which shows a balance between graphitic and disordered carbon components in the material. The C-K-edge X-ray absorption near-edge structure (XANES) analysis was conducted to determine the electronic state of carbon in NiMoC (Fig. 2f). The peaks at 288 eV and 290 eV correspond to carbide and σ* C—H, respectively, indicating the presence of the Mo—C bond. [49–51] The doublet peaks at 293 eV and 300 eV as well as the peak at 284.7 eV show the σ* C—C and π* C=C, due to graphite-like and disordered carbon components. [52,53]

Based on the characterisation results, the sputtered NiMoC contains NiMo, amorphous Mo_2C, graphite, and disordered carbons. This highlights the unique capability of magnetron co-sputtering with separate carbon source to generate multiple components in a single-step synthesis, successfully producing graphite and Mo_2C at room temperature.

3.3. *Electrochemical performance of NiMoC in alkaline condition*

Linear sweep Voltammetry (LSV) was conducted to examine the HER performance of the developed catalysts in 1 M KOH (pH = 13.5) at room temperature. To optimise the HER performance, we evaluated the impact of Mo%, thickness, and C% by varying the power of the targets and deposition time. First, the atomic ratio of Mo was optimised by adjusting the Mo target power, achieving a Ni to Mo ratio of 5.66, which corresponds to 15 % Mo content (Fig. S8a). This value is in line with findings from previous studies. Next, the thickness of the NiMo layer was optimised by varying the deposition time, with the optimal thickness determined to be 700 nm (Fig. S8b). The increased thickness enhances catalytic availability within the porous network, but exceeding 700 nm reduces performance, consistent with previous findings. [46] Fig. S8c demonstrates that the optimal composition of NiMoC is achieved with 10 % carbon, adjusted by regulating the power of the graphite target. This composition results in a significant improvement in overpotential, with reductions of 62.8 % at 10 mA cm^{-2} (OP_{10}) and 20.1 % at 100 mA cm^{-2} (OP_{100}) compared to NiMo alone.

Fig. 3a illustrates the LSV performance of optimised NiMoC (Opt NiMoC) with 90 % iR correction, showing overpotentials of 26 mV at 10 mA cm^{-2} (OP_{10}) and 168 mV at 100 mA cm^{-2} (OP_{100}). Compared to optimum NiMo (Opt NiMo), NiMoC demonstrates a 62.8 % improvement at OP_{10}. The performance is also 72.6 % better than MoC and 79.4 % better than NiC at OP_{10}. At 100 mA cm^{-2} (OP_{100}), NiMoC shows a 20.1 % improvement over Opt NiMo, with performance enhancements of 27.7 % compared to MoC and 36.0 % compared to NiC, further highlighting its effectiveness as a catalyst. The superior performance of NiMoC compared to NiMo and MoC demonstrates their synergistic effect on HER, highlighting the importance of using three different magnetron sputtering targets. Additionally, sputtered Pt deposited on PNF is used as a benchmark to assess the performance of the developed NiMoC against the top-performing HER catalyst. The comparison reveals that NiMoC outperforms sputtered Pt at high current densities, particularly above 210 mA cm^{-2}, making it more suitable for industrial electrolysis applications. To ensure the repeatability of the developed NiMoC, the experiment was repeated two more times, yielding consistent results, as depicted in Figs. S9a and b.

Furthermore, NiMoC exhibits a smaller Tafel slope, as determined from LSV analysis, compared to NiMo, MoC, and NiC (Fig. 3b). This reduction in Tafel slope indicates that the carbon addition alters the mechanism from Volmer-Heyrovský to Volmer-Tafel, which can enhance the rate of H_2 generation. [54]. EIS indicates that NiMoC displays the lowest charge transfer resistance among tested catalysts (Fig. 3c), while their ohmic resistance remains unchanged. This reduction can be attributed to the generation of Mo—C, graphite and disordered carbon, enhancing catalytic activity and conductivity, respectively. [55]

C_{dl} serves as a reliable indicator of the electrochemically active surface area. [15] The incorporation of carbon increases the C_{dl} by 1.59 times, from 10.9 mF cm^{-2} for NiMo to 17.3 mF cm^{-2} for NiMoC, consequently enhancing catalytic activity (Fig. S10). To explore charge transfer properties, we conducted multi-current chronopotentiometry of NiMoC, with gradually increasing the current density from 50 mA cm^{-2} to 300 mA cm^{-2}. Remarkably, the potential promptly stabilises and remains constant for 5 min without remarkable fluctuations. Furthermore, identical potentials are observed during the reverse process for the same current densities, which can lead to exceptional mass transport, mechanical durability, and charge transfer properties of NiMoC (Fig. S11). [15]

Fig. 3d illustrates the long-term stability of NiMoC at 10 mA cm^{-2}, demonstrating that the catalyst remains stable for 10 days. The stability of NiMoC was assessed at a high current density of 100 mA cm^{-2}, revealing its stability for 78 h (Fig. S12). The ideal alignment between the measured faradaic efficiency of NiMoC and the calculated quantities of H_2, provides evidence of no any side reactions (Fig. S13).

Comparisons of the overpotential at 10 mA cm^{-2} and 100 mA cm^{-2} and the stability of NiMoC with recently reported carbon-based HER catalysts are shown in Fig. 3e. NiMoC demonstrates superior performance to these recent studies in both HER activity and durability. This evidence strongly suggests that NiMoC is well-suited for application in water electrolysis. [16] It is worth highlighting that our one-step magnetron sputtering process is synthesised at room temperature,

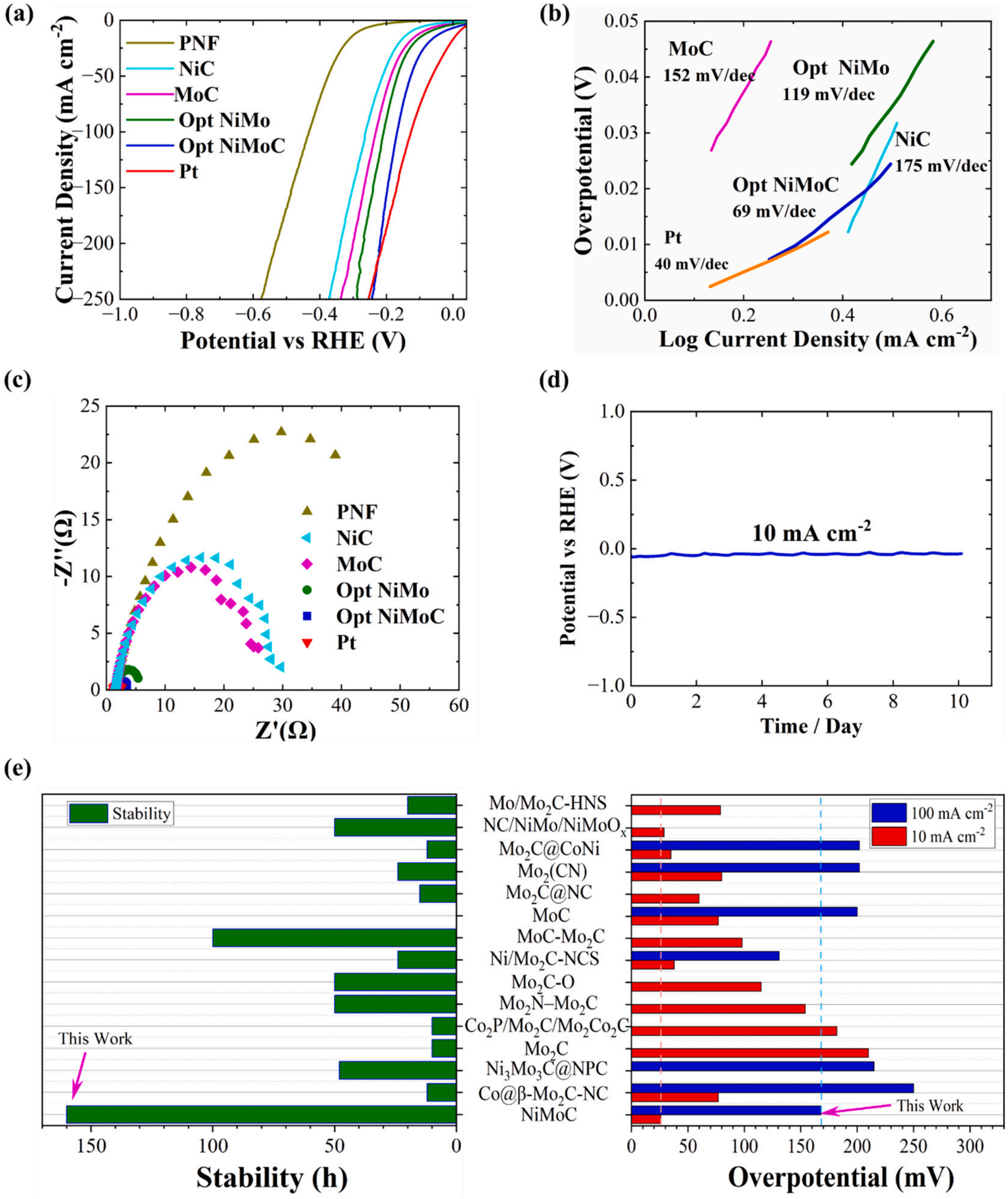

Fig. 3. Comparison of Opt NiMoC, Opt NiMo, MoC, NiC, PNF, and Pt: (a) Linear sweep voltammetry (LSV) curves in 1 M KOH, (b) Tafel plots, (c) Nyquist plot. (d) Long-term stability of NiMoC electrode at 10 mA cm^{-2} (non-iR corrected), (e) Comparison of iR-corrected OP_{10} and stability at operational current density with similar electrocatalysts.

unlike most other catalysts that require high-temperature processes. This simplicity is promising for industrial applications, ensuring scalability and ease of implementation.

3.4. Electrochemical performance of NiMoC in acidic condition

Only a few earth-abundant catalysts exhibit stability and high performance in diverse pH conditions. [56] Previous studies have highlighted the notable activity and stability of both NiMo and Mo_2C in these environments, [55,57,58] prompting us to investigate our developed sputtered NiMoC in acidic media. The HER performance of NiMoC was evaluated in 0.5 M H_2SO_4 using a standard three-electrodes system, with commercial Pt as a counter electrode. LSV curves of sputtered catalysts are displayed in Fig. 4a, revealing the superior HER activity of NiMoC by smaller OP_{10} (42 mV) compared to NiMo (83 mV), MoC (232 mV) and NiC (258 mV). Fig. 4b presents the Tafel slope of various catalysts in 0.5 M H_2SO_4 solution, analysed through LSV curves. NiMoC shows the small Tafel plot (53 mV dec^{-1}), significantly lower than NiMo (94 mV dec^{-1}), MoC (122 mV dec^{-1}) and NiC (145 mV dec^{-1}). This suggests that both NiMoC and NiMo adhere to the Volmer–Heyrovsky mechanism; However, NiMoC demonstrates a higher density of active sites and lower hydrogen coverage. [58,59]

The EIS was tested at OP_{10} to assess the resistivity of sputtered catalysts in acidic media (Fig. S14). NiMoC demonstrates the lowest charge transfer, as evidenced by the smallest semicircle observed, highlighting the impact of Mo_2C, graphite and disordered carbon generations. A chronopotentiometric measurement in 0.5 M H_2SO_4 shows that the HER performance of NiMoC remains stable for >70 h. Recent NiMo- and Mo_2C-based catalysts are compared with developed NiMoC in acidic conditions in Fig. 4d. NiMoC though is not specifically optimised in

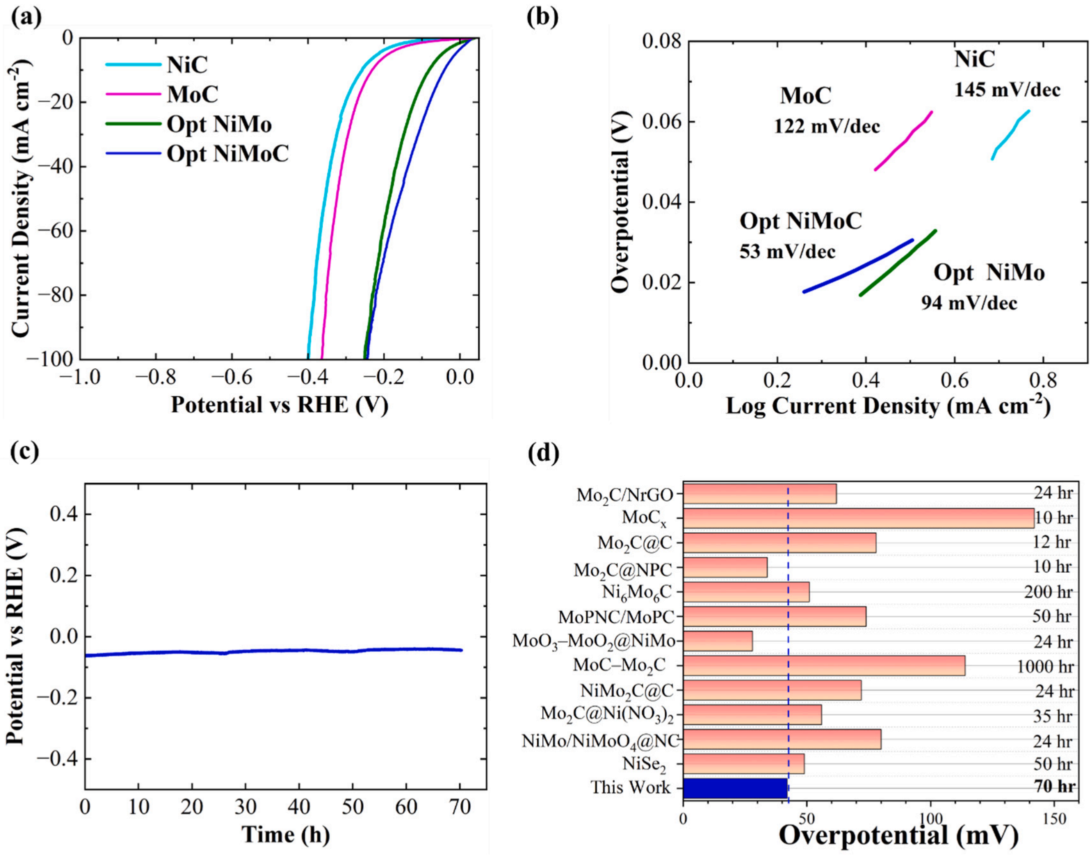

Fig. 4. (a) LSV curves of Opt NiMoC, Opt NiMo, MoC, NiC in 0.5 H_2SO_4, (b) Tafel plots of NiMoC, Opt NiMo, MoC, NiC in 0.5 M H_2SO_4. (c) Chronopotentiometric measurement of NiMoC at 10 mA cm^{-2} in 0.5 H_2SO_4 (non-iR corrected), (d) OP_{10} comparison of optimised NiMoC with recent electrocatalysts in 0.5 M H_2SO_4; stability shown on the right.

acidic conditions, shows high HER performance and stability.

Fig. S15 shows the surface morphology of NiMoC after long-term stability testing in acidic conditions. A uniform catalytic layer is observed, with no major changes except for minor agglomeration and surface roughening, which are consistent with previous reports. [60] EDS mappings (Fig. S16) confirm the uniform distribution of Ni, Mo, and C after stability testing, similar to their distribution before the test (Fig. S5b).

Fig. S17 compares the valence band spectra of Ni, Mo, and C before and after long-term stability testing. After stability, the Ni^+ signal disappears, and Ni^{3+} and Ni^{3+} satellite peak (Ni^{3+}, sat.) appears, likely due to electrochemical oxidation and surface adaptation in acidic condition. The proportion of metallic Ni^0 also increases, which may enhance HER activity. XPS results for Mo 3d indicate that Mo^0 is oxidised under acidic conditions, leading to an increased proportion of Mo^{4+} and Mo^{6+}. The C 1 s spectra remain unchanged, indicating that the Mo—C bond in NiMoC remains stable. Based on the XPS peak areas of Ni 2p, Mo 3d, and C 1 s (at 283.4 eV), the atomic ratio of Ni:Mo:C after stability is approximately 10.55:2.05:1. This is close to the ratio reported in Section 3.2. ICP-MS was used to quantify metal loss. Before the test, the Ni and Mo contents were 217 μg and 77 μg, corresponding to an atomic ratio of Ni:Mo of 4.61:1. After the test, the contents slightly decreased to 198 μg and 72 μg, with a corresponding atomic ratio of 4.49:1. This corresponds to only 8.7 % Ni loss and 6.5 % Mo loss, suggesting only minor leaching of Ni and Mo. These results indicate minor metal leaching during HER testing in acidic conditions, without significant changes in structure or composition, consistent with previous findings on similar Ni-based catalysts under acidic conditions. [42,55,58] The retained atomic ratio indicates that the working catalyst remains NiMoC-based, with only slight deviation (Ni_xMoC), which does not notably affect its performance.

3.5. *Electrochemical performance of NiMoC in neutral condition*

The HER performance of Opt NiMoC is evaluated in a 1 M PBS solution using a three-electrode system at room temperature (Fig. S18a). The LSV of Opt NiMoC shows an overpotential of 168 mV at 10 mA cm^{-2} without iR correction and 152 mV with 90 % iR correction, which are lower than those of NiMo (210 mV) and PNF (406 mV). The improved charge transfer resistance of Opt NiMoC compared to NiMo is confirmed by electrochemical impedance spectroscopy (EIS) (Fig. S18b). Chronopotentiometric measurements demonstrate the long-term stability of Opt NiMoC at 10 mA cm^{-2} under neutral conditions (Fig. S18c). A comparison of the LSV curves before and after stability testing shows a slight increase in overpotential by 25 mV at 10 mA cm^{-2} (Fig. S18d). The overpotential of Opt NiMoC is also compared to similar catalysts in the literature under neutral conditions (Table S3), highlighting its high catalytic performance achieved through one-step triple magnetron co-sputtering.

Magnetron sputtering allows simultaneous deposition of multiple elements and adding a graphite target leads to developing the active components without multi-steps or complex synthesis procedures. Our sputtered NiMoC exhibits excellent performance for HER across various pH ranges. Notably, it achieved an OP_{10} of 26 mV in basic media and 42 mV in acidic media, with impressive stability durations of 10 days and 70 h, respectively. These findings highlight the effectiveness of our straightforward technique in producing efficient TMMCs catalysts at room temperature. Also, this breakthrough carries immense potential for advancing diverse energy conversion systems, promising substantial improvements in energy conversion systems.

3.6. Zero-gap electrolyser cell

We evaluated our developed NiMoC in zero-gap alkaline water electrolyser to assess its performance at high current densities surpassing 500 mA cm^{-2}, typical in industrial electrolysers. The zero-gap design minimises losses from electrolyte and gas bubble resistances by reducing the gap between the anode and cathode electrodes. [61] This setup also accelerates gas bubble dissociation, leading to enhanced overall performance. [16,62] Fig. 5a depicts a schematic illustration of the zero-gap electrolyser, illustrating the separation of HER and OER electrodes by an anion exchange membrane. The HER electrodes consist of sputtered NiMoC on PNF, while the OER electrode is comprised of NiFeCo, developed in our group. [22]

Fig. 5b presents LSV plots at various electrolyte temperatures, acquired within a potential range of 1.2–2.0 V using a scanning rate of 50 mV s^{-1}. The water electrolysis begins at a cell voltage of 1.65 V at room temperature and decreases to 1.55 V when the electrolyte temperature is increased to 70 °C. The remarkable catalytic activities of NiMoC result in low cell voltages of 1.89 V, 1.85 V, and 1.78 V to achieve the current density of 0.5 A cm^{-2} at room temperature, 50 °C, and 70 °C, respectively. In addition, for a current density of 1 A cm^{-2}, the cell voltage is 1.99 V, 1.95 V, and 1.87 V at room temperature, 50 °C, and 70 °C, respectively, highlighting the superior performance of NiMoC even at higher current density. Fig. S19 shows the overpotential at 0.5 A cm^{-2} and 1 A cm^{-2} achieved from Fig. 5b in different temperatures. The increase in current density with rising electrolyte temperature is due to improved reaction kinetics and higher membrane conductivity. [63] This phenomenon becomes notably prominent above 50 °C, attributed to the enhanced electrolyte conductivity and the Ni-based catalyst's electrical conductivity. [64] This performance surpasses that of the benchmark Pt–C/IrO_2 electrode pair, which typically demands a voltage of 2.25 V. [65]

Fig. 5c depicts the impressive stability of the electrolyser cell at 0.5 A cm^{-2} and 40 °C, showing the stable performance over 68 h. In Fig. 5d, the unchanged LSV of the system at 40 °C, before and after this period of stability, underscores the durability of the developed NiMoC catalyst under high current density conditions. The cell voltage achieved at 0.5 A cm^{-2} is compared with recent studies that employed a similar setup but with different electrodes, using 1 M KOH (Fig. S20 and Table S4). It is evident that our developed NiMoC, in combination with NiFeCo, exhibits performance comparable to that of the Pt-NiFeCo system previously evaluated by our group under similar conditions. [22] This highlights the significant potential of sputtered NiMoC to serve as a viable alternative to Pt as one of the most effective HER catalysts.

The comparison, alongside the noteworthy performance, validates the potential application of our developed sputtered NiMoC in industrial electrolysis. This opens avenues for depositing NiMoC by facile magnetron sputtering onto substrates rather than directly onto the membrane. Consequently, this facilitates the straightforward redeposition of a fresh NiMoC layer without necessitating the replacement of expensive membranes.

4. Conclusion

We successfully developed high-performance and cost-effective NiMoC for HER water splitting, synthesised using one-step magnetron co-sputtering at room temperature. By introducing a separate carbon source during sputtering, we achieved precise control over the NiMoC composition. The optimised NiMoC catalyst exhibits an overpotential of 26 mV with a durability of 10 days under alkaline conditions, representing a 62.8 % improvement compared to NiMo. This performance results from the synergistic effects of NiMo and Mo_2C for the HER, while

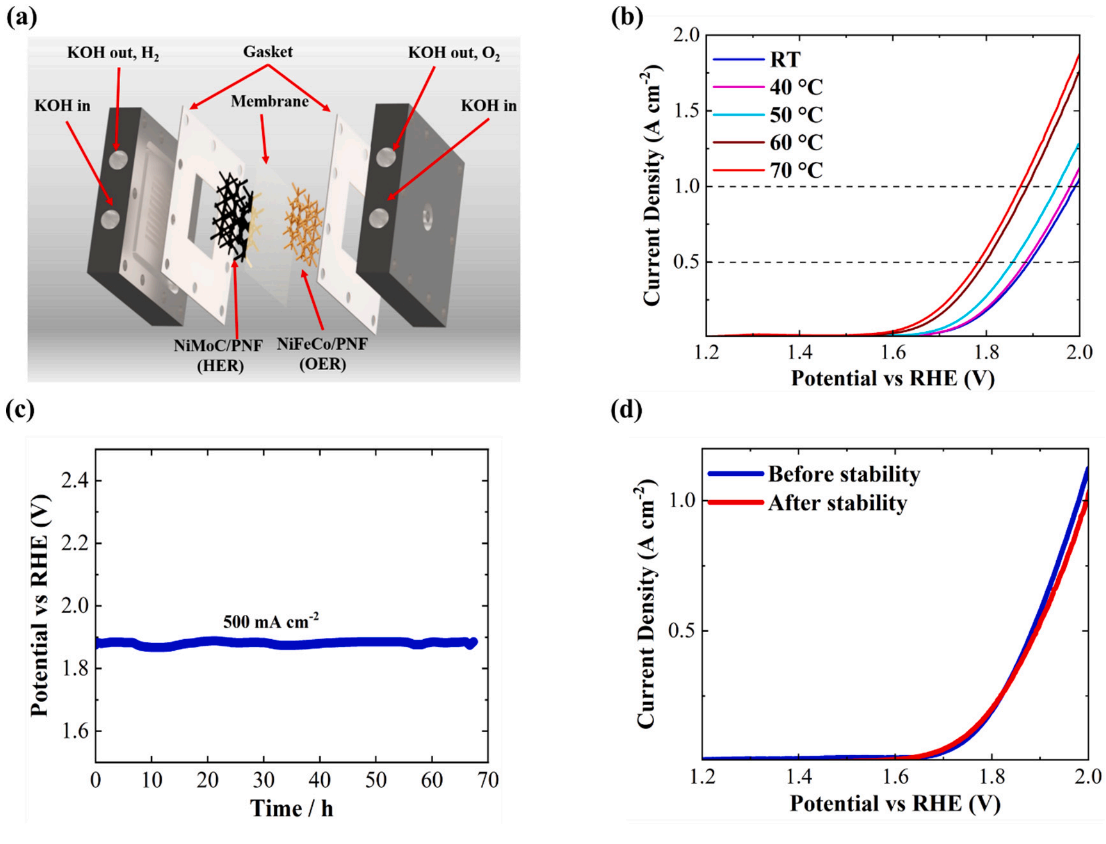

Fig. 5. (a) Schematic of zero-gap electrolyser cell for assessing performance under high current densities. (b) LSV curves of NiMoC-NiFeCo in zero-gap alkaline water electrolyser with different electrolyte temperatures. (c) long-term stability of NiMoC-NiFeCo in the electrolyser device at 500 mA cm^{-2}. (d) LSV curves of NiMoC-NiFeCo electrodes in zero-gap electrolyser before and after stability tests.

the presence of disordered and graphite-like carbon improves conductivity and stability. Moreover, sputtered NiMoC demonstrates superior performance in diverse pH conditions showing potential for use in both alkaline and acidic electrolysers. It achieves an overpotential of 42 mV at 10 mA cm^{-2} and maintains stable operation for 70 h in acidic conditions. It exhibits outstanding performance when integrated into a zero-gap alkaline electrolyser, achieving a cell voltage of 1.78 V at 0.5 A cm^{-2} and 1.87 V at 1 A cm^{-2}. This study highlights the potential of magnetron sputtering to engineer and develop high-performance TMMC catalysts at room temperature. Our findings pave the way for more efficient and scalable production of catalysts, enhancing the feasibility of water splitting and other energy conversion technologies.

CRediT authorship contribution statement

Farid Attar: Writing – original draft, Validation, Software, Formal analysis, Data curation, Conceptualization. **Asim Riaz:** Writing – review & editing, Methodology, Formal analysis. **Doudou Zhang:** Writing – review & editing, Methodology, Data curation. **Haijiao Lu:** Methodology, Conceptualization. **Lars Thomsen:** Methodology, Conceptualization. **Siva Karuturi:** Writing – review & editing, Supervision, Conceptualization.

Declaration of competing interest

The authors declare that they have no known competing financial interests or personal relationships that could have appeared to influence the work reported in this paper.

Acknowledgements

The authors gratefully acknowledge funding support from the Australian Renewable Energy Agency and the Australian Research Council. Dr. Zhang acknowledges the funding support from the Macquarie University Research Fellowships. Part of this research was undertaken on the SXR beamline at the Australian Synchrotron, part of ANSTO.

Appendix A. Supplementary data

Supplementary data to this article can be found online at https://doi.org/10.1016/j.cej.2025.164494.

Data availability

No data was used for the research described in the article.

References

[1] F. Attar, H. Yin, S.L. Schumann, J. Langley, N. Cox, Z. Zeng, K. Catchpole, S. Karuturi, Z. Yin, Advanced electron paramagnetic resonance in chemical energy conversion: current status and future potential, Energy Environ. Sci. 17 (10) (2024) 3307–3328.

[2] M.R. Karimi Estahbanati, N. Mahinpey, M. Feilizadeh, F. Attar, M.C. Iliuta, Kinetic study of the effects of pH on the photocatalytic hydrogen production from alcohols, Int. J. Hydrog. Energy 44 (2019) 32030–32041.

[3] Z. Wu, Q. Li, G. Xu, W. Jin, W. Xiao, Z. Li, T. Ma, S. Feng, L. Wang, Microwave phosphine-plasma-assisted ultrafast synthesis of halogen-doped Ru/RuP2 with surface intermediate adsorption modulation for efficient alkaline hydrogen evolution reaction, Adv. Mater. 36 (2024) 2311018.

[4] G. Liu, Y. Xu, T. Yang, L. Jiang, Recent advances in electrocatalysts for seawater splitting, Nano Mater. Sci. 5 (2023) 101–116.

[5] Q. Gao, Z. Wang, W. Gao, H. Yin, NiFeCo-based high entropy alloys nanoparticles coated with N-doped graphene layers as hydrogen evolution catalyst in alkaline solution, Chem. Eng. J. 489 (2024) 151370.

[6] D. Zhang, J.Z. Soo, H.H. Tan, C. Jagadish, K. Catchpole, S.K. Karuturi, Earth-abundant amorphous Electrocatalysts for electrochemical hydrogen production: a review, Adv. Energy Sustain. Res. 2 (2021) 2000071.

[7] J. Yang, H. Xuan, J. Yang, X. Liang, Y. Li, J. Yang, P. Han, Bimetallic NiMo oxides coupled with 3D CuxO nanorods for efficient overall water splitting, J. Alloys Compd. 934 (2023) 167908.

[8] Y.-N. Zhou, W.-L. Yu, H.-J. Liu, R.-Y. Fan, G.-Q. Han, B. Dong, Y.-M. Chai, Self-integration exactly constructing oxygen-modified MoNi alloys for efficient hydrogen evolution, EcoEnergy 1 (2023) 425–436.

[9] M.S.A. Sher Shah, G.Y. Jang, K. Zhang, J.H. Park, Transition metal carbide-based nanostructures for electrochemical hydrogen and oxygen evolution reactions, EcoEnergy 1 (2023) 344–374.

[10] H. Fiedler, N. Malone, D.R.G. Mitchell, M. Nancarrow, V. Jovic, G.I.N. Waterhouse, J. Kennedy, P. Gupta, Room temperature ion beam synthesis of ultra-fine molybdenum carbide nanoparticles: toward a scalable fabrication route for earth-abundant electrodes, Small 20 (2024) 2304118 n/a.

[11] B. Deng, Z. Wang, W. Chen, J.T. Li, D.X. Luong, R.A. Carter, G. Gao, B.I. Yakobson, Y. Zhao, J.M. Tour, Phase controlled synthesis of transition metal carbide nanocrystals by ultrafast flash joule heating, Nat. Commun. 13 (2022) 262.

[12] F. Yu, Y. Gao, Z. Lang, Y. Ma, L. Yin, J. Du, H. Tan, Y. Wang, Y. Li, Electrocatalytic performance of ultrasmall Mo2C affected by different transition metal dopants in hydrogen evolution reaction, Nanoscale 10 (2018) 6080–6087.

[13] P. Chen, J. Ye, H. Wang, L. Ouyang, M. Zhu, Recent progress of transition metal carbides/nitrides for electrocatalytic water splitting, J. Alloys Compd. 883 (2021) 160833.

[14] J. Liang, Q. Liu, T. Li, Y. Luo, S. Lu, X. Shi, F. Zhang, A.M. Asiri, X. Sun, Magnetron sputtering enabled sustainable synthesis of nanomaterials for energy electrocatalysis, Green Chem. 23 (2021) 2834–2867.

[15] F. Attar, A. Sharma, B. Gupta, S. Karuturi, Statistical design-guided synthesis of Nanoarchitectonics of high-performance NiFeMoN Electrocatalyst through facile one-step magnetron sputtering, Adv. Sci. 11 (2024) 2308063.

[16] D. Zhang, H. Li, A. Riaz, A. Sharma, W. Liang, Y. Wang, H. Chen, K. Vora, D. Yan, Z. Su, A. Tricoli, C. Zhao, F.J. Beck, K. Reuter, K. Catchpole, S. Karuturi, Unconventional direct synthesis of Ni3N/Ni with N-vacancies for efficient and stable hydrogen evolution, Energy Environ. Sci. 15 (2022) 185–195.

[17] J. Ni, J. Li, J. Jian, J. He, H. Chen, X. Leng, X. Liu, Recent studies on the fabrication of multilayer films by magnetron sputtering and their irradiation behaviors, Coatings 11 (2021) 1468.

[18] G. Zhu, B. Xiao, G. Chen, Z. Gan, Study on the deposition uniformity of triple-target magnetron co-sputtering system: numerical simulation and experiment, Materials 15 (2022) 7770.

[19] X. Cao, A. Jiang, S. Tao, J. Liu, J. Xiao, Structure and electrocatalytic hydrogen evolution performance of Mo2C thin films prepared by magnetron sputtering, Int. J. Hydrog. Energy 48 (2023) 24196–24206.

[20] Z. Liu, J. Ai, M. Sun, F. Han, Z. Li, Q. Peng, Q.-D. Wang, J. Liu, L. Liu, Phosphorous-doped graphite layers with outstanding Electrocatalytic activities for the oxygen and hydrogen evolution reactions in water electrolysis, Adv. Funct. Mater. 30 (2020) 1910741.

[21] Z. Pu, R. Cheng, J. Zhao, Z. Hu, C. Li, W. Li, P. Wang, I.S. Amiinu, Z. Wang, W. Min, D. Chen, S. Mu, Anion-modulated platinum for high-performance multifunctional electrocatalysis toward HER, HOR, and ORR, iScience 23 (2020) 101793.

[22] A. Riaz, Z. Fusco, F. Kremer, B. Gupta, D. Zhang, C. Jagadish, H.H. Tan, S. Karuturi, Hierarchically multiscale vertically oriented NiFeCo Nanoflakes for efficient electrochemical oxygen evolution at high current densities, Adv. Energy Mater. 14 (2024) 2303001.

[23] S.R. Shatynski, The thermochemistry of transition metal carbides, Oxid. Met. 13 (1979) 105–118.

[24] T. Suszko, E. Dobruchowska, W. Gulbiński, G. Greczynski, J. Morgiel, B. Kawczyński, K. Załęski, K. Dorywalski, S. Pogorzelski, NiMo-C coatings synthesized by reactive magnetron sputtering for application as a catalyst for the hydrogen evolution reaction in an acidic environment, ACS Appl. Mater. Interfaces 17 (2025) 3344–3355.

[25] U. Jansson, E. Lewin, Sputter deposition of transition-metal carbide films — a critical review from a chemical perspective, Thin Solid Films 536 (2013) 1–24.

[26] W. Dai, X. Li, L. Wu, Q. Wang, Structure and properties of molybdenum-disulfide/amorphous carbon composited coatings deposited by co-sputtering method, Diam. Relat. Mater. 101 (2020) 107643.

[27] E.J. Liang, J.W. Zhang, J. Leme, C. Moura, L. Cunha, Raman analysis of Si–C–N films grown by reactive magnetron sputtering, Thin Solid Films 469-470 (2004) 410–415.

[28] Y. Xu, M.J. Dzara, S. Kabir, S. Pylypenko, K. Neyerlin, A. Zakutayev, X-ray photoelectron spectroscopy and rotating disk electrode measurements of smooth sputtered Fe-N-C films, Appl. Surf. Sci. 515 (2020) 146012.

[29] L. Ciambriello, E. Cavaliere, I. Vassalini, I. Alessandri, M. Ferroni, L. Leoncino, R. Brescia, L. Gavioli, Role of electrode thickness in NiFe Nanogranular films for oxygen evolution reaction, J. Phys. Chem. C 126 (2022) 21759–21770.

[30] M. Yang, H. Zhu, Y. Zheng, C. Zhang, G. Luo, Q. Xu, Q. Li, S. Zhang, T. Goto, R. Tu, One-step chemical vapor deposition fabrication of Ni@NiO@graphite nanoparticles for the oxygen evolution reaction of water splitting, RSC Adv. 12 (2022) 10496–10503.

[31] J. Ding, D. Zhang, A. Riaz, H. Gu, J. Zheyan Soo, P. Reddy Narangari, C. Jagadish, H. Hoe Tan, S. Karuturi, Scalable amorphous NiFe(OH)x/Fe/graphene bifunctional electrocatalyst via solution-corrosion for water splitting, CCS Chem. 0 (2024) 1–12.

[32] D. Zhang, Q. Ma, H. Fan, H. Yang, S. Liu, Millimeter-long multilayer graphene nanoribbons prepared by wet chemical processing, Carbon 71 (2014) 120–126.

[33] P. Wang, R. Qin, P. Ji, Z. Pu, J. Zhu, C. Lin, Y. Zhao, H. Tang, W. Li, S. Mu, Synergistic coupling of Ni nanoparticles with Ni3C Nanosheets for highly efficient overall water splitting, Small 16 (2020) 2001642.

[34] J. Liu, J. Huang, J. Sun, Y. Song, J. Yang, Q. Chen, X. Zhang, L. Zhang, Rapid synthesis of NiMo-based electrocatalysts at room temperature for efficient oxygen and hydrogen evolution in seawater, J. Electroanal. Chem. 935 (2023) 117311.

[35] L. Huo, C. Jin, K. Jiang, Q. Bao, Z. Hu, J. Chu, Applications of nickel-based Electrocatalysts for hydrogen evolution reaction, Adv. Energy Sustain. Res. 3 (2022) 2100189.

[36] J. Ni, Z. Ruan, J. Xu, J. Yan, J. Ma, H. Ma, J. Qi, S. Zhu, L. Lu, Regulating surface wettability and electronic state of molybdenum carbide for improved hydrogen evolution reaction, Int. J. Hydrog. Energy 48 (2023) 17478–17488.

[37] H. Shi, Y.-T. Zhou, R.-Q. Yao, W.-B. Wan, X. Ge, W. Zhang, Z. Wen, X.-Y. Lang, W.-T. Zheng, Q. Jiang, Spontaneously separated intermetallic Co3Mo from nanoporous copper as versatile electrocatalysts for highly efficient water splitting, Nat. Commun. 11 (2020) 2940.

[38] L. Wang, X. Duan, X. Liu, J. Gu, R. Si, Y. Qiu, Y. Qiu, D. Shi, F. Chen, X. Sun, J. Lin, J. Sun, Atomically dispersed Mo supported on metallic Co9S8 Nanoflakes as an advanced Noble-metal-free bifunctional water splitting catalyst working in universal pH conditions, Adv. Energy Mater. 10 (2020) 1903137.

[39] X. Qian, J. Fang, J. Xia, G. He, H. Chen, Recent progress and perspective on molybdenum-based electrocatalysts for water electrolysis, Int. J. Hydrog. Energy 48 (2023) 26084–26106.

[40] Y. Xu, J. Yang, T. Liao, R. Ge, Y. Liu, J. Zhang, Y. Li, M. Zhu, S. Li, W. Li, Bifunctional water splitting enhancement by manipulating Mo-H bonding energy of transition metal-Mo2C heterostructure catalysts, Chem. Eng. J. 431 (2022) 134126.

[41] A.A. Smirnov, Z. Geng, S.A. Khromova, S.G. Zavarukhin, O.A. Bulavchenko, A. A. Saraev, V.V. Kaichev, D.Y. Ermakov, V.A. Yakovlev, Nickel molybdenum carbides: synthesis, characterization, and catalytic activity in hydrodeoxygenation of anisole and ethyl caprate, J. Catal. 354 (2017) 61–77.

[42] L. Guo, J. Wang, X. Teng, Y. Liu, X. He, Z. Chen, A Novel Bimetallic Nickel–Molybdenum Carbide Nanowire Array for Efficient Hydrogen Evolution, ChemSusChem 11 (2018) 2717–2723.

[43] X. Xu, F. Nosheen, X. Wang, Ni-Decorated Molybdenum Carbide Hollow Structure Derived from Carbon-Coated Metal–Organic Framework for Electrocatalytic Hydrogen Evolution Reaction, Chem. Mater. 28 (2016) 6313–6320.

[44] S. Liu, C. Sun, J. Chen, J. Xiao, J.-L. Luo, A High-Performance Ruddlesden–Popper Perovskite for Bifunctional Oxygen Electrocatalysis, ACS Catal. 10 (2020) 13437–13444.

[45] P. Kumar, S.K. Maity, D. Shee, Role of NiMo alloy and Ni species in the performance of NiMo/alumina catalysts for Hydrodeoxygenation of stearic acid: a kinetic study, ACS Omega 4 (2019) 2833–2843.

[46] V.R. Jothi, K. Karuppasamy, T. Maiyalagan, H. Rajan, C.-Y. Jung, S.C. Yi, Corrosion and alloy engineering in rational Design of High Current Density Electrodes for efficient water splitting, Adv. Energy Mater. 10 (2020) 1904020.

[47] M. He, H. Shi, P. Wang, X. Sun, B. Gao, Porous molybdenum carbide nanostructures synthesized on carbon cloth by CVD for efficient hydrogen production, Chem. Eur. J. 25 (2019) 16106–16113.

[48] X. Du, J. Liu, D. Li, H. Xin, X. Lei, R. Zhang, L. Zhou, H. Yang, Y. Zeng, H. Zhang, W. Zheng, X. Wen, C. Hu, Structural and electronic effects boosting Ni-doped Mo2C catalyst toward high-efficiency CO/CC bonds cleavage, J. Energy Chem. 75 (2022) 109–116.

[49] Z. Shi, K. Nie, Z.-J. Shao, B. Gao, H. Lin, H. Zhang, B. Liu, Y. Wang, Y. Zhang, X. Sun, X.-M. Cao, P. Hu, Q. Gao, Y. Tang, Phosphorus-Mo2C@carbon nanowires toward efficient electrochemical hydrogen evolution: composition, structural and electronic regulation, Energy Environ. Sci. 10 (2017) 1262–1271.

[50] Y. Huang, Q. Gong, X. Song, K. Feng, K. Nie, F. Zhao, Y. Wang, M. Zeng, J. Zhong, Y. Li, Mo2C nanoparticles dispersed on hierarchical carbon microflowers for efficient Electrocatalytic hydrogen evolution, ACS Nano 10 (2016) 11337–11343.

[51] J.G. Chen, B. Frühberger, J. Eng, B.E. Bent, Controlling surface reactivities of transition metals by carbide formation, J. Mol. Catal. A Chem. 131 (1998) 285–299.

[52] F. Pan, W.-l. Wang, D. Chen, W. Yan, Influence of *LiFePO4*/C interface on electrochemical properties, J. Mater. Chem. 21 (2011) 14680–14684.

[53] J. Zhou, X. Zhou, X. Sun, R. Li, M. Murphy, Z. Ding, X. Sun, T.-K. Sham, Interaction between Pt nanoparticles and carbon nanotubes – an X-ray absorption near edge structures (XANES) study, Chem. Phys. Lett. 437 (2007) 229–232.

[54] S. Anantharaj, S. Noda, V.R. Jothi, S. Yi, M. Driess, P.W. Menezes, Strategies and perspectives to catch the missing pieces in energy-efficient hydrogen evolution reaction in alkaline media, Angew. Chem. Int. Ed. 60 (2021) 18981–19006.

[55] P. Xiao, Y. Yan, X. Ge, Z. Liu, J.-Y. Wang, X. Wang, Investigation of molybdenum carbide nano-rod as an efficient and durable electrocatalyst for hydrogen evolution in acidic and alkaline media, Appl. Catal. B Environ. 154-155 (2014) 232–237.

[56] B. Zhou, J. Wang, L. Guo, H. Li, W. Xiao, G. Xu, D. Chen, C. Li, Y. Du, H. Ding, Y. Zhang, Z. Wu, L. Wang, Microwave-assisted PtRu alloying on defective tungsten oxide: a pathway to improved hydroxyl dynamics for highly-efficient hydrogen evolution reaction, Adv. Energy Mater. 14 (2024) 2402372.

[57] A. Nadar, A.M. Banerjee, M.R. Pai, R.P. Antony, A.K. Patra, P.U. Sastry, H. Donthula, R. Tewari, A.K. Tripathi, Effect of Mo content on hydrogen evolution reaction activity of Mo2C/C electrocatalysts, Int. J. Hydrog. Energy 45 (2020) 12691–12701.

[58] F. Bao, E. Kemppainen, I. Dorbandt, R. Bors, F. Xi, R. Schlatmann, R. van de Krol, S. Calnan, Understanding the hydrogen evolution reaction kinetics of electrodeposited nickel-molybdenum in acidic, near-neutral, and alkaline conditions, ChemElectroChem 8 (2021) 195–208.

[59] S. Anantharaj, S.R. Ede, K. Karthick, S. Sam Sankar, K. Sangeetha, P.E. Karthik, S. Kundu, Precision and correctness in the evaluation of electrocatalytic water splitting: revisiting activity parameters with a critical assessment, Energy Environ. Sci. 11 (2018) 744–771.

[60] R. de Paz-Castany, K. Eiler, A. Nicolenco, M. Lekka, E. García-Lecina, G. Brunin, G.-M. Rignanese, D. Waroquiers, T. Collet, A. Hubin, E. Pellicer, Hydrogen evolution reaction of electrodeposited Ni-W films in acidic medium and performance optimization using machine learning, ChemSusChem 18 (2025) e202400444.

[61] Y. Song, W. Xie, M. Shao, X. Duan, Integrated electrocatalysts derived from metal organic frameworks for gas-involved reactions, Nano Mater. Sci. 5 (2023) 161–176.

[62] F. Attar, A. Riaz, P. Reddy Narangari, J. Zheyan Soo, S. Karuturi, Statistical analysis and comprehensive optimisation of zero-gap electrolyser: transitioning catalysts from laboratory to industrial scale, Chem. Eng. J. 498 (2024) 155486.

[63] F. Rocha, R. Delmelle, C. Georgiadis, J. Proost, Effect of pore size and electrolyte flow rate on the bubble removal efficiency of 3D pure Ni foam electrodes during alkaline water electrolysis, J. Environ. Chem. Eng. 10 (2022) 107648.

[64] S.M. Bashir, M.A. Nadeem, M. Al-Oufi, M. Al-Hakami, T.T. Isimjan, H. Idriss, Sixteen percent solar-to-hydrogen efficiency using a power-matched alkaline Electrolyzer and a high concentrated solar cell: effect of operating parameters, ACS Omega 5 (2020) 10510–10518.

[65] C.-L. Huang, K. Sasaki, D. Senthil Raja, C.-T. Hsieh, Y.-J. Wu, J.-T. Su, C.-C. Cheng, P.-Y. Cheng, S.-H. Lin, Y. Choi, S.-Y. Lu, Twinning enhances efficiencies of metallic catalysts toward electrolytic water splitting, Adv. Energy Mater. 11 (2021) 2101827.